

Post-buckled precompressed subsonic micro-flight control actuators and surfaces

Ron Barrett and Roelof Vos

Aerospace Engineering Department, The University of Kansas, Lawrence, KS, USA

E-mail: adaptivebarrett@yahoo.com

Received 28 January 2008, in final form 10 July 2008

Published 5 August 2008

Online at stacks.iop.org/SMS/17/055011

Abstract

This paper describes a new class of flight control actuators using post-buckled precompressed (PBP) piezoelectric elements to provide much improved actuator performance. These PBP actuator elements are modeled using basic large deflection Euler-beam estimations accounting for laminated plate effects. The deflection estimations are then coupled to a high rotation kinematic model which translates PBP beam bending to stabilator deflections. A test article using PZT-5H piezoceramic sheets built into an active bender element was fitted with an elastic band which induced much improved deflection levels. Statically the bender element was capable of producing unloaded end rotations on the order of $\pm 2.6^\circ$. With axial compression, the end deflections were shown to increase nearly four-fold. The PBP element was then fitted with a graphite–epoxy aeroshell which was designed to pitch around a tubular stainless steel main spar. Quasi-static bench testing showed excellent correlation between theory and experiment through $\pm 25^\circ$ of pitch deflection. Finally, wind tunnel testing was conducted at airspeeds up to 120 kts (62 m s^{-1} , 202 ft s^{-1}). Testing showed that deflections up to $\pm 20^\circ$ could be maintained at even the highest flight speed. The stabilator showed no flutter or divergence tendencies at all flight speeds. At higher deflection levels, it was shown that a slight degradation deflection was induced by nose-down pitching moments generated by separated flow conditions induced by extremely high angles of attack.

(Some figures in this article are in colour only in the electronic version)

Nomenclature

			y	Out-of-plane displacement dimension	mm (in)
a	Integrating factor	(—)	z	Through thickness dimension	mm (in)
A, B, D	In-plane, coupled, bending laminate stiffnesses	N m^{-1} , N, N m (lb/in, lb, in lb)	<i>Greek symbols</i>		
b	Actuator width	mm (in)	α	Angle of attack	deg
c	Integrating factor	(—)	δ	PBP beam angle	deg
c	Chord	mm (in)	δ_0	PBP end rotation angle	deg
E	Stiffness or electric field	GPa (msi), V m^{-1} (V in^{-1})	ϕ	Stabilator pitch angle	deg
L_L	Lever arm length	mm (in)	ϵ	Laminate in-plane strain	μstrain
L_0	Actuator element length	mm (in)	κ	Laminate curvature	rad in^{-1} (rad m^{-1})
$L_{0\text{tot}}$	Total actuator and extension length	mm (in)	Λ	Piezoelectric free element strain	μstrain
M	Applied moment vector	N m m^{-1} (in lb in $^{-1}$)	σ	Stress	MPa (ksi)
N	Applied force vector	N m^{-1} (lb in $^{-1}$)	<i>Subscripts</i>		
t	Thickness	mm (in)	a	Actuator	
			b	Bond	
			e	End	

ex External
 l Laminate
 s Substrate

1. Introduction

For more than 20 years, the aerospace engineering and adaptive structures communities have been regularly experimenting with classes of active materials and devices which are intended for flight control. Starting in the mid-1980s, early concepts of adaptive flight control actuators used active materials like piezoelectric ceramic sheets to bend and twist solid state lifting surfaces [1]. Since that time, many studies have centered on trading force for stroke, most often to amplify small commanded strain levels and arrive at larger motions [2–7]. Although trading force for stroke has been shown to generate large deflections, the total work density and actuator efficiencies are inherently degraded because some finite amount of total work is lost in the conversion. Additionally, the apparatus which enables the trading of force for stroke adds cost and complexity, and because mass is also added, the actuator bandwidth is also reduced. One family of solutions to the amplification dilemma involves the use of highly active single-crystal piezoelectric elements. These elements need far less amplification as they can command strain levels in excess of 1.7% [8]. Although an elegant solution, the costs of such elements are orders of magnitude greater than those of many other families of piezoceramic sheets, plates and stacks. Because they are so cost-prohibitive, they have unfortunately not yet been integrated into successful flight control mechanisms. Like many industries, the aerospace industry often places severe weight, volume and cost constraints on actuator elements for aircraft of all scales. Additionally, bandwidth, power consumption and reliability are also crucial. Accordingly, there is a constant drive to find ‘ever better’ classes of actuators for every scale of aircraft. Among the most demanding aircraft classes are small uninhabited aerial vehicles and micro-aerial vehicles (MAVs). These aircraft encounter very adverse scaling properties and have very high gross weight to component weight sensitivities because of subscale flow properties and structural design and fabrication considerations. To help blunt the adverse effects of these scaling factors, several classes of piezoelectric flight control actuators have been developed for these aircraft [9–11]. Figure 1 shows the first MAV which was commissioned in 1994 by the DoD CounterDrug Office and was enabled by piezoelectric Flexspar flight control actuators.

Several families of subscale aircraft have since followed the Kolibri and have very successfully employed various classes and incarnations of piezoelectrically activated flight control mechanisms. One of the more noteworthy is the XQ-138 [12]. The XQ-138 is designed to take-off and land vertically, hover like a helicopter, then pitch over and transition to airplane-mode flight for dash out, cruise, and loiter to speeds in excess of several hundred knots. Because this class of convertible uninhabited aerial vehicle (CUAV) is also intended to operate in urban and forested environments in any type

of weather, the demands on the flight control assembly are extremely high. Accordingly, one of the primary purposes of this paper is to introduce the technical community to another incarnation of flight control actuator which is capable of handling the low speed flight regimes of the Kolibri and also the very high speed, robust post-stall maneuvering flight modes of the XQ-138. Prior to 2003, all of the adaptive flight control schemes employed force-for-stroke trading actuator designs. These actuator concepts most often used laminated piezoelectric sheets which would expand or contract several hundred microstrain and ultimately generate peak rotations on the order of 10° of some form of control surface. Figure 2 shows a comparison of control surface performance from the mid-1990s.

Although effective, these schemes were extremely limited because adaptive actuators typically have almost no moment generating capability as they approach the limits of their stroke. This necessitated a design point which was typically half the maximum stroke and half the maximum blocked moment which could be generated. Because the design for typical flight control actuators was so compromised, much of the ultimate capability of the actuator was fundamentally missed. Figure 3 shows a typical design space boundary superimposed upon the stabilator performance curve for a Flexspar stabilator.

Because nearly all actuators of this era (and most in use today) traded force for stroke, their mass normalized power density was considerably below that of the raw material. This deflection–stroke barrier was nearly impossible to penetrate until a new method of approaching piezoelectric actuation was conceived. The overall concept of this new method is to employ an apparatus around a piezoelectric actuator element which allows for the simultaneous expansion of both force and stroke capabilities. The first incarnation of this paradigm-shifting actuation scheme was in an electrical transformer designed by Lesieutre and Davis [13, 14]. The pair of investigators showed that by applying axial forces to a piezoelectric bender element just under the inactive buckling load, they could drive the coupling coefficient to nearly 1, which of course indicates that the electrical-to-mechanical conversion efficiency was increased multifold. Although counterintuitive (and often disputed), it was handily shown that the coupling coefficient of the system was significantly higher than that of the material itself. Since these early years of experimentation with PBP actuators, many other advances have followed. In 2003, several PBP flight control concepts were generated, reduced to practice and included in an international patent application [15]. Once filed and claims were allowed, publication followed, including works on convertible UAVs and morphing wings. In every case, it was shown that the PBP concept was significantly superior to conventional ‘force for deflection’ approaches [16–19]. Although the concepts presented in [16–19] are good and appropriate for the classes of aircraft demonstrated on, the original Kolibri stabilator technology had yet to be updated. Accordingly, this paper describes a new incarnation of this, now old, flight control mechanism



Figure 1. The Lutronix Kolibri, the world’s first VTOL MAV enabled by piezoelectric flexspar stabilators (1997) [12].

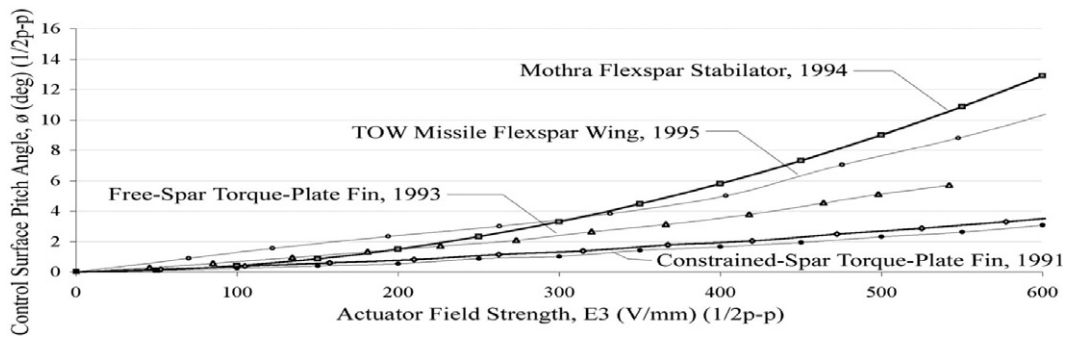


Figure 2. Comparison of flight control surface deflection performance using conventional adaptive actuators schemes.

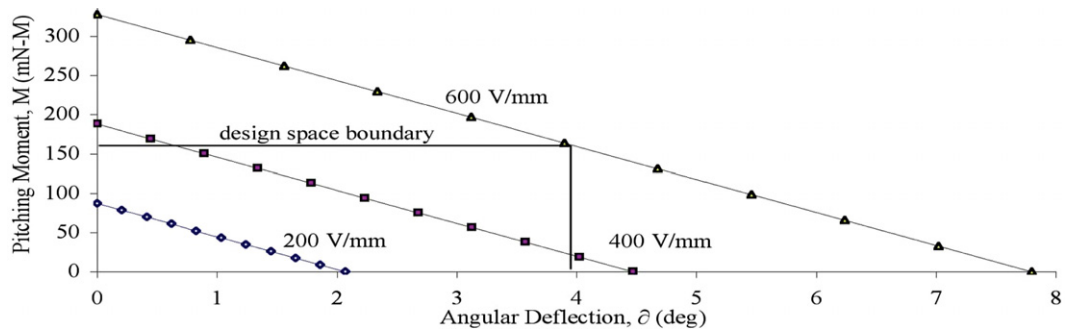


Figure 3. Characteristic force–deflection design space for a conventional piezoelectric flight control actuator.

which, with PBP technology, exhibits dramatically improved performance.

2. Analytic modeling

2.1. Generic actuator set-up

The most generic PBP actuator is constructed with an active sandwich beam at the core and axial loads applied at the ends. Although pin–pin configurations are most common, partially rotationally constrained actuators have also been explored. As the axial force is increased, the beam is pushed closer to its linear inactive buckling load (i.e., without imperfections), but generally not over it. As the axial force increases, small commanded bending imperfections generated by adaptive actuators lead to higher deflections. Figure 4 shows the PBP actuation scheme.

2.2. PBP actuator element modeling

From [16–19], it can be seen that several major approaches to modeling PBP actuators can be successfully employed. The first modeling techniques which appropriately captured the performance of PBP actuator elements employed a combination of classical laminated plate theory (CLPT) and Euler beams with an accounting for large deformations [16, 18]. A second approach used energy methods and assumed mode shapes to capture post-buckled beam performance [17, 19]. Finally, finite element methods were also used to determine PBP behavior [19]. For ‘classical’ PBP actuator elements, the quickest, accurate method to determine element behavior is to employ a closed-form estimation of performance.

The basic closed-form model to capture PBP behavior relies upon 20 years of experience. One important aspect

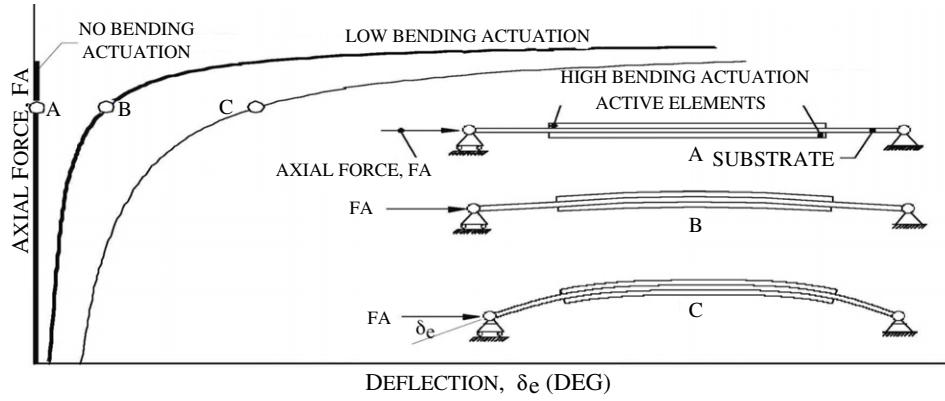


Figure 4. Generic arrangement of a post-buckled precompressed (PBP) actuator arrangement.

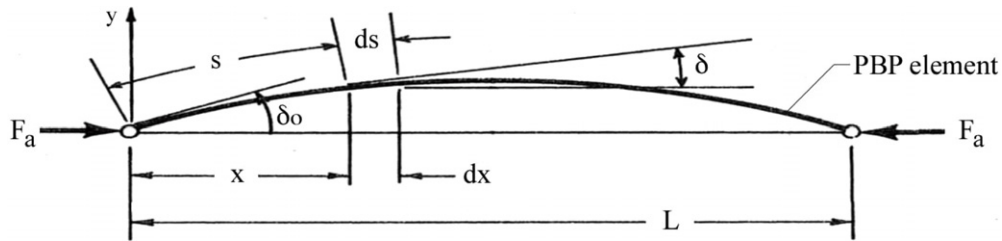


Figure 5. Terms and conventions for analysis of the PBP actuator arrangement.

of the design relies upon coefficient of thermal expansion (CTE) mismatch between the substrate and the active elements. This CTE mismatch allows the piezoceramics to be placed in compression and a (normally isotropic metal) substrate to be placed in tension. When cured at an elevated temperature, the resulting laminate becomes much more resistant to both depoling and fracture on the tension face. By using the techniques laid out in [20], the resultant forces and moments in the laminate are obtained by integrating the stress over the thickness of the laminate. These techniques generate performance points along the horizontal axis of figure 4:

$$N = \int \sigma dz \quad M = \int \sigma z dz. \quad (1)$$

Actuator in-plane forces and moments (a) can be expressed as a balance with external forces and moments (ex) and forces and moments due to mismatches in coefficients of thermal expansion (t). These factors will generate in-plane laminate strains, ϵ and curvatures, κ :

$$\begin{pmatrix} N \\ M \end{pmatrix}_a + \begin{pmatrix} N \\ M \end{pmatrix}_{ex} + \begin{pmatrix} N \\ M \end{pmatrix}_t = \begin{bmatrix} A & B \\ B & D \end{bmatrix}_1 \begin{pmatrix} \epsilon \\ \kappa \end{pmatrix}_1. \quad (2)$$

Because free element bending of a balanced, symmetric PBP beam is not generally manipulated by active elements, both externally applied and thermally induced forces and moments can be neglected as follows:

$$\begin{bmatrix} A & B \\ B & D \end{bmatrix}_a \begin{pmatrix} \Lambda \\ 0 \end{pmatrix}_a = \begin{bmatrix} A & B \\ B & D \end{bmatrix}_1 \begin{pmatrix} \epsilon \\ \kappa \end{pmatrix}_1. \quad (3)$$

At this point, equation (3) can be easily solved for laminate longitudinal curvature, Λ , by assuming that a balanced,

symmetric laminate composed of isotropic or quasi-isotropic elements with a zero stiffness bond are used with actuator thickness, t_a , bond thickness, t_b , substrate thickness, t_s , actuator stiffness, E_a , and substrate stiffness, E_s , as follows:

$$\kappa_{11} = \frac{E_a(t_s t_a + 2t_b t_a + t_a^2)}{\left(\frac{E_s t_s^3}{12}\right) + E_a \left\{ \left[\frac{t_a(t_s + 2t_b)^2}{2} \right] + (t_s + 2t_b)t_a^2 + \frac{2}{3}t_a^3 \right\}} \Lambda_1. \quad (4)$$

By using the unloaded laminate curvature, κ_{11} , as a starting point, the problem can now be defined in terms of gross curvatures with an externally applied axial force, F_a , as shown in figure 5.

Figure 5 shows that the length along the surface of the element, s , and the length along the major axis of the element, x , are related by the curvature induced in the actuator. The angular coordinate, δ , is maximized at the ends of the element, δ_o , and goes to zero at the mid-point.

One can consider the normal strain of any point in the PBP actuator at a distance y from the neutral axis through its thickness as

$$\epsilon = \frac{y d\delta}{ds} = \frac{\sigma}{E}. \quad (5)$$

If one examines the individual beam element and assumes pure bending, then the following holds:

$$\sigma = \frac{My}{I}. \quad (6)$$

Accordingly, combining equations (5) and (6) with CLPT conventions and terminology, equation (7) is obtained:

$$\frac{y d\delta}{ds} = \frac{My}{D_1 b}. \quad (7)$$

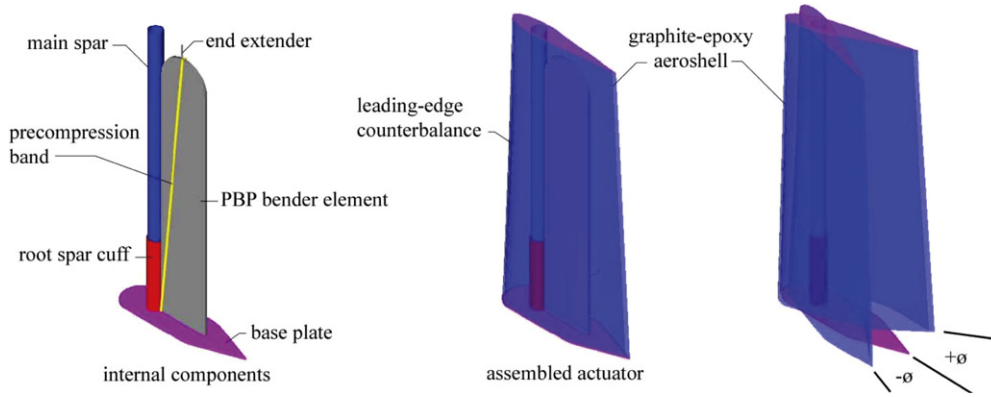


Figure 6. Typical arrangement of a tip-joint flexspar stabilator with an elastic-enabled PBP actuator.

The externally applied moment loading in each section comes from the axial force, F_a . Therefore

$$M = -F_a y. \quad (8)$$

Substituting equation (8) into (7) yields

$$\frac{d\delta}{ds} = \frac{-F_a y}{D_1 b}. \quad (9)$$

Differentiating equation (9) with respect to s :

$$\frac{d^2\delta}{ds^2} = -\frac{F_a}{D_1 b} \sin \delta. \quad (10)$$

Multiplying through by the integration factor $2 d\delta/ds$:

$$2 \frac{d\delta}{ds} \frac{d^2\delta}{ds^2} = -2 \frac{F_a}{D_1 b} \sin \delta \frac{d\delta}{ds}. \quad (11)$$

Integrating equation (11) with respect to s :

$$\left(\frac{d\delta}{ds}\right)^2 = 2 \frac{F_a}{D_1 b} \cos \delta + a. \quad (12)$$

If one considers the addition of an applied moment via piezoelectric elements as generating an imperfection across the beam, then the unknown integrating factor, a , can be solved for, given that at $x = 0$, $\delta = \delta_0$, $d\delta/ds = \kappa_{11} = \kappa$

$$a = 2 \frac{F_a}{D_1 b} (\cos \delta - \cos \delta_0) + \kappa^2. \quad (13)$$

With appropriate trigonometric substitutions, and considering the negative root because $d\delta$ is always negative,

$$\frac{d\delta}{ds} = -2 \sqrt{\frac{F_a}{D_1 b} \sqrt{\sin^2\left(\frac{\delta_0}{2}\right) - \sin^2\left(\frac{\delta}{2}\right) + \frac{\kappa^2 D_1 b}{4 F_a}}}. \quad (14)$$

For solution, a change of variable is made as follows:

$$\sin\left(\frac{\delta}{2}\right) = c \sin \xi; \quad (15)$$

where ξ is a variable with the value $\pi/2$ when $x = 0$ and the value 0 when $x = L/2$. Accordingly, when $x = 0$,

$$c = \sin\left(\frac{\delta_0}{2}\right). \quad (16)$$

Solving for δ and differentiating yields

$$\delta = 2 \sin^{-1} \left(\sin\left(\frac{\delta_0}{2}\right) \sin \xi \right), \quad (17)$$

$$d\delta = \frac{2 \sin\left(\frac{\delta_0}{2}\right) \cos \xi}{\sqrt{1 - \sin^2\left(\frac{\delta_0}{2}\right) \sin^2 \xi}} d\xi.$$

Combining equations (14)–(17) with appropriate end values:

$$\sqrt{\frac{F_a}{D_1 b}} \int_0^{L/2} ds = \frac{L}{2} \sqrt{\frac{F_a}{D_1 b}}$$

$$= \int_0^{\pi/2} \frac{\sin\left(\frac{\delta_0}{2}\right) \cos \xi}{\left(\sqrt{\sin^2\left(\frac{\delta_0}{2}\right) \cos^2 \xi + \frac{\kappa^2 D_1 b}{4 F_a}}\right) \left(\sqrt{1 - \sin^2\left(\frac{\delta_0}{2}\right) \sin^2 \xi}\right)} d\xi. \quad (18)$$

Accordingly, the closed-form solution shown in equation (18) accounts for large geometric rotations and will be shown to accurately capture the performance of PBP actuator elements.

2.3. Integrated actuator analytical modeling and kinematics

By drawing upon early Flexspar designs from the 1990s, significant improvements in performance can be induced by switching from conventional active bender elements to PBP bender elements. Figure 6 shows the layout of a typical tip-joint flexspar stabilator with an elastic-enabled PBP actuator within.

From figure 6 it can be seen that the aeroshell freely rotates around the main spar. In most cases, the main spar is simply a piece of tubular stainless steel (hypodermic needle tubing) for small scales and pultruded graphite–epoxy tubing for larger scales. For the largest scale actuators, the arrangement is switched from a sleeve bearing to a roller-pin bearing arrangement. Several important geometric features are seen to dominate the performance of the actuator. Figure 7 lays out the nomenclature.

By using the nomenclature laid out in figure 7 and the kinematics of [21], a simple relationship can be solved which relates the geometry of figure 7 with equation (18). Several

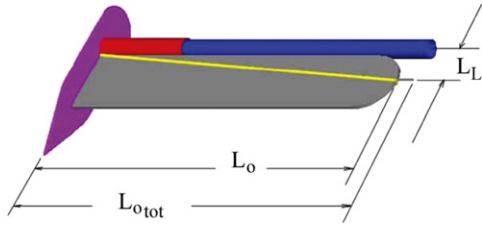


Figure 7. Tip-joint flexspar stabilator principal geometric parameter nomenclature.

important assumptions are made in developing the following relation, including: (1) the lever distance, L_L , is essentially unchanged through the entire rotation, (2) the curvature of the element is constant and follows a circular arc profile, and (3) friction, stiction and slop effects are not included.

$$\phi = 2 \sin^{-1} \left[\frac{1 - \cos(\delta_0)}{2\delta_0 \left(\frac{L_L}{L_o}\right)} + \left(\frac{L_{o_{tot}}}{2L_L} - \frac{\sin(\delta_0)}{2\delta_0 \left(\frac{L_L}{L_o}\right)} \right) \sin(\delta_0) \right]. \quad (19)$$

Although all three of the above assumptions are not representative of the ‘real’ world, the following sections will show that such effects are second order at best and the modeling techniques described above are suitable for engineering modeling.

3. Actuator design and fabrication

The actuator element was constructed from a sandwich of two sheets of PZT-5H piezoceramic laminated to a steel substrate. Figure 8 shows the overall geometry, thickness and material distribution of the element.

The actuator element was constructed from two sheets of tape-cast PZT-5H piezoceramic sheets bonded to either side of a $76 \mu\text{m}$ (3 mil) AISI 1010 steel substrate with Scotchweld adhesive tape. The element was electrically connected to the substrate by MasterBond EP21TDC-N conducting epoxy. Fabrication was carried out under approximately 206 kPa (30 psi) of pressure at 177°C (350°F) cure conditions. These conditions contributed to a high level of precompression.

The element was designed with a substrate end overrun of 5 mm (0.2 in) which was brazed to an AISI 304 stainless steel base plate. The base plate was also fitted with a 2.8 mm (0.11 in) O.D. root cuff and 2.4 mm (0.095 in) O.D. main spar of AISI 304 stainless steel. Following brazing, the base was tapped to 2–56 and fitted with an 8 mm (0.314 in) long 2–56 stainless steel mounting screw. The end was tapped to 0–80 and fitted with a 6.35 mm (0.25 in) screw and washer assembly. Figure 9 shows the mechanical assembly. The internal assembly was designed to take loads up to deep stall at 120 kts in a standard atmosphere. Figure 10 shows the overall configuration and assembly of the PBP actuator.

4. Experimental testing and results

4.1. Quasi-static actuator element bench testing

The first set of tests was structured to verify the correlation between theory and experiment on the element level. Laser reflection techniques were used on the PBP actuator element itself to verify the modeling techniques embodied in section 2. The laser reflection techniques are accurate and repeatable to 0.01° and were measured at the end extender. Testing was performed at a quasi-static rate of 1 Hz. Figure 11 shows the results for the free element prior to being fitted with the aeroshell.

Figure 11 clearly shows that at higher deflection angles at high field, a significant amount of additional deflection occurs. This effect is particularly time dependent and related to actuator element creep induced by in-plane tensile stresses. Another effect is the off-axis rotation which occurs because the elastic band is not set along the line of the elastic axes.

4.2. Quasi-static stabilator bench testing

The PBP stabilator was assembled and tested using the same laser reflection techniques as used on the PBP beam itself. Testing demonstrated slop on the order of 0.17° which was observed to occur in two locations: (1) between the main spar and the sleeve bearing assembly and (2) between the end extender and socket. Although 0.17° is comparatively small as it is below 0.34% of total peak-to-peak deflections, it can be ameliorated by improved tolerances. Figure 12 shows the quasi-static test results for the entire stabilator rotation angle.

The most striking characteristic of PBP stabilator behavior shown in figure 12 is the sharp upturn in compression force at a relatively constant pitch angle of 25° at 600 V mm^{-1} . This is induced by a bump-stop feature built into the stabilator itself. As the control surface would tend to overrotate and go past 25° , it is physically prevented from doing so as the aeroshell makes contact with the side of the PBP actuator element itself. This is a safety feature intended to prevent damage to the element in the event of rough handling or gusts.

4.3. Wind tunnel testing

The PBP stabilator was wind tunnel tested through 120 kts in the 3×4 ft wind tunnel at the University of Kansas Aerospace Engineering Department. Wind tunnel testing showed no flutter or divergence tendencies, which was expected as the elastic axis of the stabilator, line of centers of gravity and line of aerodynamic centers are all collocated on the quarter-chord. Figure 13 demonstrated steady deflection trends with airspeed at low deflection levels. As the airspeed increased, high angles of attack and associated stall conditions led to nose-down pitching moments which retarded the peak deflection levels. It can also be seen that if a conventional piezoelectric actuator were to have been used, then the design space prescribed in figure 3 would limit the fully controlled, reversible deflection levels to just under 4° , as shown below.

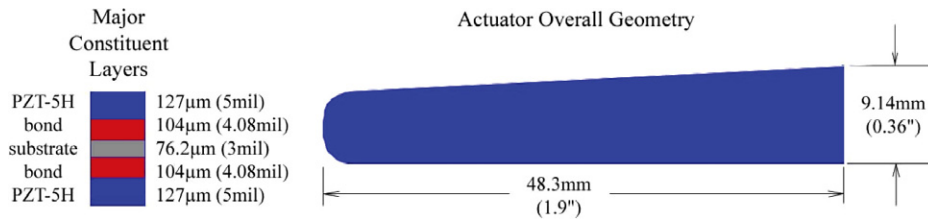


Figure 8. Overall geometry of the PBP active element.

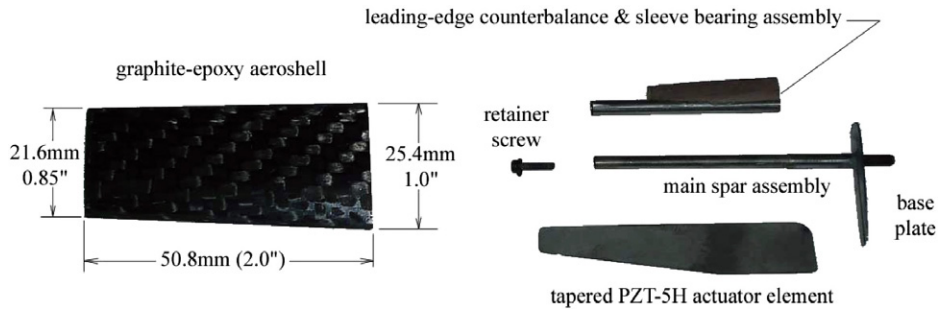


Figure 9. Components of the flexspar PBP actuator element.



Figure 10. Assembled stabilator and assembled PBP actuator core.

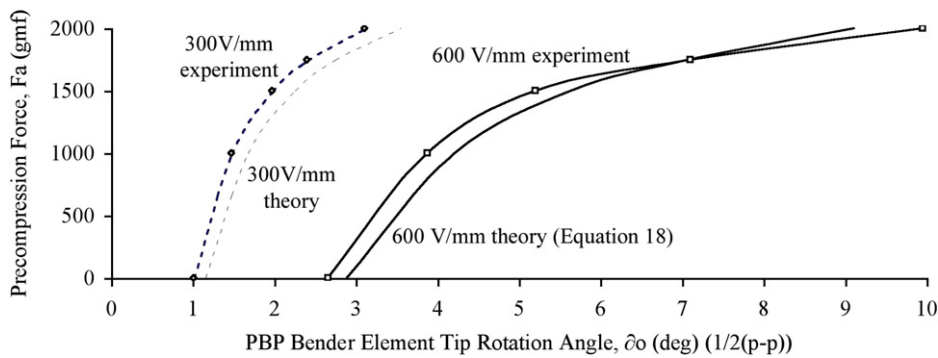


Figure 11. Comparison of Euler-beam post-buckled performance quasi-static theory and experimental test results.

From figure 13, it can be seen that the stabilator performance is right in line with many industry applications. Given that large deflections can be commanded at relatively low fields, this implies that total system voltage levels will be more compatible with conventional electronics. This is an important feature as this helps extricate small-scale subsonic adaptive flight control devices from the costly, heavy and extremely inefficient specialized high voltage electronics which are now frequently used.

4.4. Dynamics and power consumption

One of the more important characteristics of aircraft flight control mechanisms is the system-level dynamics. The actuator element itself possesses a resonant frequency on the order of 52 Hz, but more critical from an aircraft designer's perspective is the dynamics of the entire assembly. Dynamic testing was conducted both on the bench and in the wind tunnel. Results from both tests were so close that discrepancies in

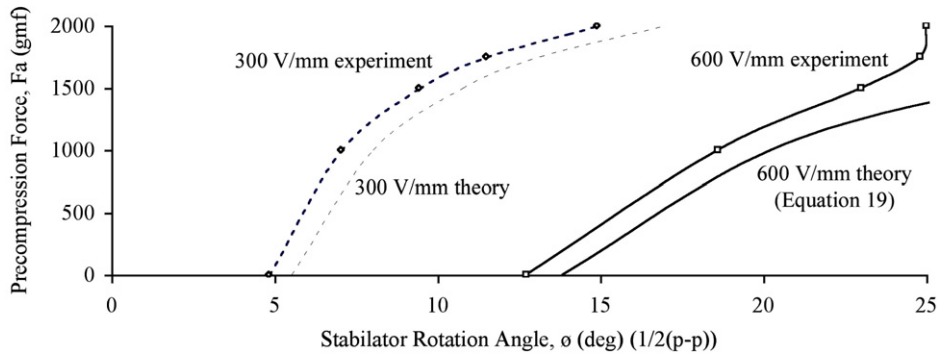


Figure 12. Comparison of PBP stabilator quasi-static theory and experimental test results.

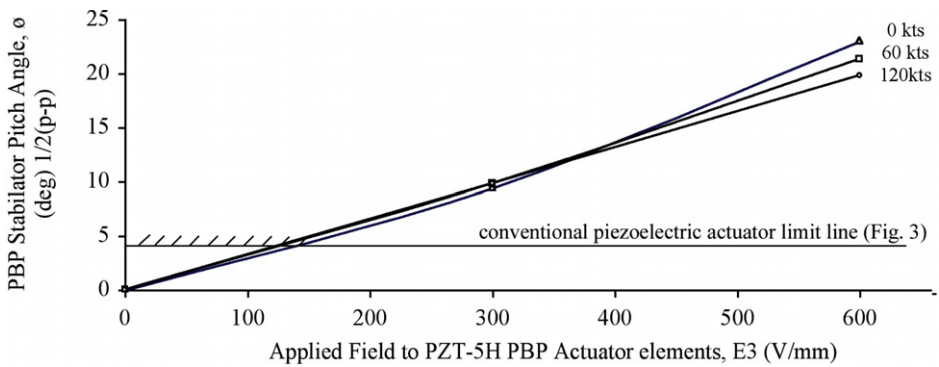


Figure 13. Wind tunnel test results.

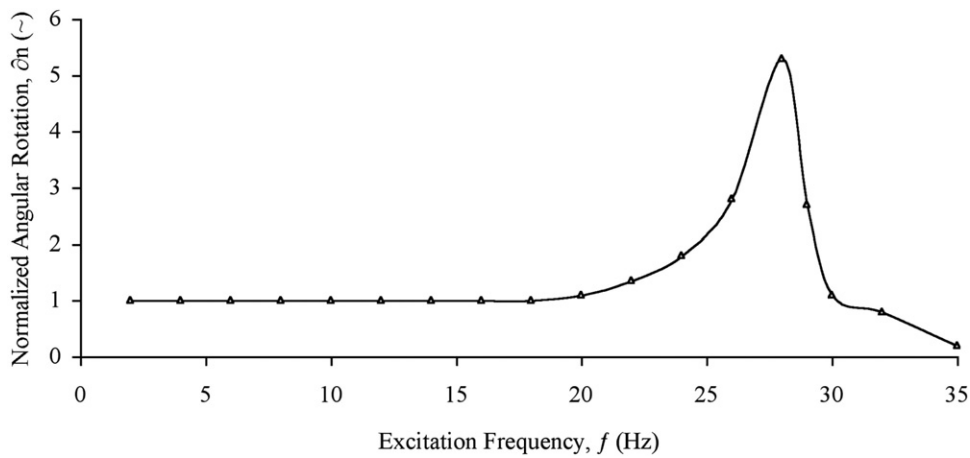


Figure 14. Stabilator dynamic response.

data sets were at the limit of the measurement equipment accuracy. The reason why airflow did not substantially affect the dynamic performance is because the high level of both inertial and aerodynamic balance and the low levels of airloads. A sinusoidal signal was applied to the stabilator and deflections were measured using laser reflection techniques. A dynamic sweep was conducted through 35 Hz and captured a natural frequency in pitch of 28 Hz with a corner frequency of approximately 33 Hz (the practical limit for flight control system designers). Figure 14 shows the dynamic response of the installed stabilator (again, both with and without airflow,

through 120 kts). Although reduced frequencies ranged up to 0.3 during tunnel testing, unsteady aerodynamic moments were clearly overpowered by actuator authority. Given a capacitance of 213 nF, the maximum power consumption recorded at maximum deflection and frequency was just under 0.04 W. It should be noted that with a static resistance of more than 20 MΩ, the quiescent current flow through the element was under 4 μA (260 μW). Experimentally it has been found that orders of magnitude more power can be expended in the power supplies and DC-DC converters themselves if proper shut-off designs are not implemented [22]. Given that the

MAV powerplants typically consume 3–5 orders of magnitude greater power, the power demands of the PBP flight control system has been rendered essentially irrelevant on an aircraft system level.

From figure 14, it is clear that the system break frequency is significantly higher than most of the short period body modes which MAVs and other subscale aircraft experience. Only a very limited number of munitions currently fly with body short period or nutation frequencies on this order of magnitude. Other issues related to flight control include stiction, friction, slop and hysteresis. By closing a simple rotational feedback loop, all of the aforementioned issues are reduced to under 0.018° . Without the feedback loop, the largest deviations between commanded and observed deflections are under 13% of peak deflection levels. From flight tests on aircraft like the Lutronix Kolibri MAV, it has been observed that aircraft using outer feedback loops are more than capable of capturing, stabilizing and controlling body attitudes to under 0.4° without the use of the inner actuator loops [23]. Still, if the need arises to stabilize to levels below 0.4° , that capability exists, but at the cost of additional loops.

4.5. Flight hardening issues

Because this system could ultimately be fielded with many different families of subscale aircraft (MAVs, guided munitions, toys, etc), several practical issues must be addressed. Among them are launch, flight mechanical, thermal and electrical hardening as well as aging. As with all flight hardened actuators, the devices must maintain structural integrity under all design conditions. To do this, the primary actuator element protection technique is to use coefficient of thermal expansion (CTE) mismatch curing techniques to precompress the piezoceramic elements from 500 to 2800 strain in-plane. This fabrication process has been shown for nearly two decades now to render otherwise fragile piezoceramic elements highly resistant to both mechanical and thermal shock in subscale aircraft experiencing instantaneous or pulse loads up to 17 000 g [24, 25]. Because the elements are to be used as 3–1 actuators rather than 3–3 actuators and are precompressed in-plane, the PZT elements also become much more resistant to depoling. Water hardening is accomplished by doping the entire actuator element with a 12–15 μm layer of oligomeric silane. Aging is an issue which has been observed to be significant not from one day or week to another, but on a multi-year basis. Because the commercial world often demands shelf lives on the order of several years and the military often specifies bunker storage durations up to 20 years, aging could be a serious issue. However, one technique which is currently used on related systems is simply to re-pole the actuators *in situ* during a preflight sequence. It should also be noted that in-plane precompression by using CTE mismatch principles reduces aging effects of the raw materials by up to an order of magnitude.

5. Conclusions

It can be concluded that a new class of actuators using axial forces to amplify otherwise small bending deflections

of piezoelectric bender elements has been successfully demonstrated in a new form of adaptive flight control surface. These post-buckled precompressed (PBP) actuator elements were modeled using basic Euler-beam and high deflection models coupled to large rotation kinematic relationships. A 5.08 cm (2 in) span, 2.54 cm (1 in) chord subscale aircraft stabilator and PBP actuator element were constructed with a high compression elastomeric band. It was shown that a simple bender element which generated only 2.6° tip rotations (unloaded) could be retrofitted with a PBP elastic to increase deflections nearly four-fold. This PBP-enabled actuator element was integrated into a graphite–epoxy aeroshell and tested quasi-statically. Pitch deflections of up to $\pm 25^\circ$ were recorded at field strengths of just 520 V mm^{-1} over the 127 μm (5 mil) thick PBP actuator elements with good correlation between theory and experiment. Wind tunnel testing of the stabilator showed no flutter or divergence tendencies and steady pitch control up to $\pm 22^\circ$ at speeds as great as 120 kts. Frequency testing demonstrated a natural frequency of 28 Hz and a corner frequency of 33 Hz.

Acknowledgments

The authors would like to acknowledge and thank Mr Wes Ellison for his help with wind tunnel repair and operation and the University of Kansas Transportation Research Institute, Aerospace Engineering Department and the Adaptive Aerostructures Laboratory for their support of this project.

References

- [1] Crawley E F and De Luis J 1987 Use of piezoelectric actuators as elements of intelligent structures *AIAA J.* **25** 987–97
- [2] Prechtl E F and Hall S R 1999 Design of a high efficiency, large stroke electromechanical actuator *J. Smart Mater. Struct.* **8** 13–30
- [3] Moskalik A J and Brei D 1998 Analytical dynamic performance modeling for individual c-block actuators *J. Vib. Acoust.* **121** 221–30
- [4] Moskalik A J and Brei D 1999 Force-deflection behavior of piezoelectric c-block actuator arrays *J. Smart Mater. Struct.* **8** 531–43
- [5] Ervin J and Brei D 1998 Recurve piezoelectric-strain-amplifying actuator architecture *IEEE/ASME Trans. Mechatron.* **3** 293–301
- [6] Clement J, Brei D, Moskalik A and Barrett R 1998 Bench-top performance characterization of a c-block driven active flap system *Proc. 39th Struct., Struct. Dynamics and Mater. Conf. (Long Beach, CA, April 1980)* (Washington, DC: American Institute of Aeronautics and Astronautics) AIAA paper no. 98-2039
- [7] Schwartz R W, Laoratanakul P, Nothwang W D, Ballato J, Moon Y and Jackson A 2000 Understanding mechanics and stress effects in rainbow and thunder actuators *Proc. Society of Photo-Optical Instrumentation Engineers (SPIE) Ann. Int. Symp. on Smart Structures and Materials; Proc. SPIE* **3992** 363–75
- [8] Anon 2007 Single crystal piezoelectrics *Data Sheet* (Pennsylvania: TRS Ceramics, State College)
- [9] Barrett R, Burger C and Melian J 2001 Recent advances in uninhabited aerial vehicle (UAV) flight control with adaptive aerostructures *Proc. 4th European Demonstrators Conf.*

- (Edinburgh, Scotland, Dec. 2001) (Bristol: Institute of Physics Publishing) pp 1–11
- [10] Barrett R and Lee G 2000 Design criteria, aircraft design, fabrication and testing of sub-canopy and urban micro-aerial vehicles *Proc. AIAA/AHS Int. Powered Lift Conf. (Alexandria, VI, Nov. 2000)* (Washington, DC: American Institute of Aeronautics and Astronautics)
- [11] Barrett R and Stutts J 1998 Development of a piezoceramic flight control surface actuator for highly compressed munitions *Proc. 39th Struct., Structural Dynamics and Mater. Conf. (Long Beach, CA, April 1998)* (Washington, DC: American Institute of Aeronautics and Astronautics) AIAA paper no. 98-2034
- [12] Barrett R 2004 Adaptive aerostructures, improving high performance, subscale military UAVs *Proc. 45th AIAA/ASME/ASCE/AHS/ASC Struct., Structural Dynamics and Mater. Conf., 12th AIAA/ASME/AHS Adaptive Struct. Conf. (Palm Springs, CA, April 2004)* (Washington, DC: American Institute of Aeronautics and Astronautics) AIAA paper no. 2004-1886
- [13] Lesieutre G A and Davis C L 1997 Can a coupling coefficient of a piezoelectric actuator be higher than those of its active material? *J. Intell. Mater. Syst. Struct.* **8** 859–67
- [14] Lesieutre G and Davis C 2001 Transfer having a coupling coefficient higher than its active material *US Patent Specification* 6,236,143 May 2001
- [15] Barrett R M and Tiso P 2005 PBP Adaptive actuator device and embodiments *International Patent Number* PCT/NL2005/000054
- [16] Barrett R, Vos R, Tiso P and De Breuker R 2005 Post-buckled precompressed (PBP) actuators: enhancing VTOL autonomous high speed MAVs *Proc. 46th AIAA/ASME/ASCE/AHS/ASC Struct., Structural Dynamics and Mater. Conf. (Austin, TX, April 2005)* (Washington, DC: American Institute of Aeronautics and Astronautics) AIAA paper no. 2005-2113
- [17] Vos R, De Breuker R, Barrett R and Tiso P 2007 Morphing wing flight control via post-buckled precompressed piezoelectric actuators *AIAA J. Aircr.* **44** 1060–9
- [18] Barrett R, McMurtry R, Vos R, Tiso P and De Breuker R 2006 Post-buckled precompressed piezoelectric flight control actuator design, development and demonstration *J. Smart Mater. Struct.* **15** 1323–31
- [19] De Breuker R, Vos R, Barrett R and Tiso P 2006 Nonlinear semi-analytical modeling of post-buckled precompressed (PBP) piezoelectric actuators for uav flight control *Proc. 47th AIAA/ASME/ASCE/AHS/ASC Struct., Structural Dynamics, and Mater. Conf., 14th AIAA/ASME/AHS Adaptive Struct. Conf. (Newport, Rhode Island, May 2006)* (Washington, DC: American Institute of Aeronautics and Astronautics) AIAA paper no. 2006-1795
- [20] Jones R M 1975 *Mechanics of Composite Materials* (New York: Hemisphere)
- [21] Barrett R M, Gross R S and Brozoski F T 1997 Design and testing of a subsonic all-moving adaptive flight control surface *AIAA J.* **35** 1217–9
- [22] Anon. 2008 Series A/SM surface mount and plug-in DC–DC converters *Pico Electronics Product Catalog* (Pelham, NY: Pico Electronics)
- [23] Barrett R 1997 *Lutronix Micro Aerial Vehicle, 'Kolibri' Final Report (Sept. 1997)* (Del Mar, CA: Lutronix Corporation)
- [24] Stutts J and Barrett R 1998 Development and experimental validation of a barrel-launched adaptive munition *Proc. 39th AIAA/ASME/ASCE/AHS/ASC Struct., Structural Dynamics, and Mater. Conf. (Long Beach, CA, April 1998)* (Washington, DC: American Institute of Aeronautics and Astronautics) AIAA paper no. 98-2037
- [25] Barrett R and Stutts J 1997 Modeling, design and testing of a barrel-launched adaptive munition *Proc. 4th Ann. Society of Photo-Optical Instrumentation Engineers Symp. on Smart Structures and Materials; Proc. SPIE* **3041** 578–89